2024 IEEE International Conference on Robotics and Automation (ICRA 2024)
May 13-17, 2024. Yokohama, Japan

Envibroscope: Real-Time Monitoring and Prediction of Environmental Motion for Enhancing Safety in Robot-Assisted Microsurgery

Alireza Alikhani[1,2], Satoshi Inagaki[1,3], Shervin Dehghani[2], Mathias Maier[1], Nassir Navab[4] and M. Ali Nasseri[1,2]

***Abstract*— Several robotic systems have emerged in the recent past to enhance the precision of micro-surgeries such as retinal procedures. Significant advancements have recently been achieved to increase the precision of such systems beyond surgeon capabilities. However, little attention has been paid to the impact of non-predicted and sudden movements of the patient and the environment. Therefore, analyzing environmental motion and vibrations is crucial to ensuring the optimal performance and reliability of medical systems that require micron-level precision, especially in real-life scenarios.**

To address this challenge, this paper introduces a novel environmental motion analysis system that employs a grid layout with distributed sensing nodes throughout the environment. This system effectively tracks undesired movements (motions) at designated locations and predicts upcoming motions using neural network-based approaches. The outcomes of our experiments exhibit promising prospects for real-time motion monitoring and prediction, which has the potential to form a solid basis for enhancing the automation, safety, integration, and overall efficiency of robot-assisted micro-surgeries.

***Index Terms*— Robot Safety, AI for Medical Robotics; Medical Robots and Systems; Sensor-Based Navigation;**

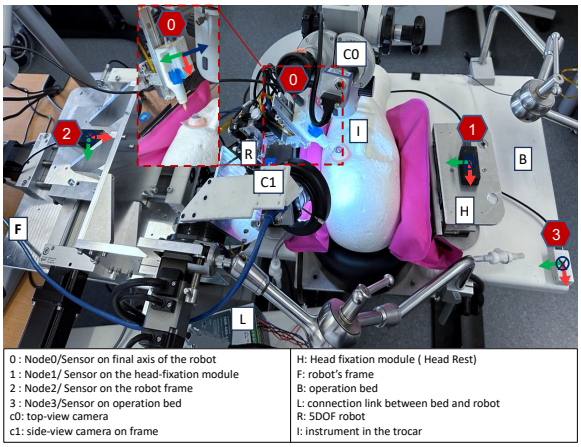

Fig. 1. Setup of the system, which shows the arrangement of the robot, head fixation module, robot's frame, and operation bed. node0, node1, node2, and node3 represent sensors placed on the final robot axis (instrument), patient head, robot's cart, and operation bed.

I. Introduction

The field of ophthalmology is noticing a wave of novel therapeutic protocols that hold immense promise for advancing eye care. However, these innovative approaches often need to be added to human surgeons' capabilities. Researchers are actively exploring ways to leverage innovative technologies, such as robotic platforms, to empower a broader range of surgeons to successfully undertake these complex procedures. Recent advances in robotics have brought exciting possibilities to improve eye surgery. These innovations go beyond traditional methods, opening doors to new treatments like gene and stem-cell therapies. These therapies require precise delivery within the delicate anatomical structures of the eye, a challenge that robotic systems are well-equipped to address [1]–[7], therefore, these robotic systems are developed to navigate and manipulate small and fragile anatomies such as retina with a total thickness of 200 to 500 um [8] including sub 10 um dimensional inner retinal membrane, and capillaries and epiretinal membrane of 60 um [9]. Hence the required accuracy for a robotic system capable of targeted delivery for retinal procedures is down to micron-level and is reported between 10-20 um [10], [11]. Several robotic systems are available with evaluated performance in lab environments that potentially can offer the required precision [12]–[17]. However, little attention has been paid to the negative effect of undesired motions and vibrations in actual clinical settings, including instances of the patient's head motion, abrupt adjustments to the surgical bed, and movements of the robot's final axis (Fig. 1). However, relatively little emphasis has been placed on the damaging effects of undesired motions and vibrations in actual clinical settings, including instances of the patient's head motion, abrupt adjustments to the surgical bed, and movements of the robot's final axis. A particular challenge arises from the patient's head motion, which is common during retinal surgeries performed under monitored anesthesia, [18], conscious sedation while the patient is often awake. In this state, head motion can result from activities like breathing, talking, and other unintended motions, with potential deviations in a range of 1-7 mm in various directions [19]. Another origin of motion during eye surgery is the patient's snoring. About 16 percent of patients under local anesthesia experience snoring, and half may exhibit sudden

This work was supported by the State of Bavaria "Bayerische Forschungsstiftung".

Corresponding author: Alireza Alikhani (alireza.alikhani@tum.de)

[1] A. Alikhani, S. Inagaki, M. Maier, and M. Ali Nasseri are with Medical Autonomy and Precision Surgery Laboratory at the ophthalmology department of the Technische Universität München, Germany.

[2] A. Alikhani, S. Dehghani, and M. Ali Nasseri are with the Department of Computer Science, Technische Universität München, Germany.

[3] Inagaki is with NSK Ltd., Japan.

[4] N. Navab is a full professor and head of the Chair for Computer Aided Medical Procedures & Augmented Reality, Technische Universität München, Germany. , and an adjunct professor at the Whiting School of Engineering, Johns Hopkins University, Baltimore, MD, USA.

movements [20]. Moreover, highly skilled and dedicated OR personnel are susceptible to errors and may add any sudden motion to the patient [21]. These errors are often unrelated to technical skill, training, or knowledge but indicate cognitive, system, or teamwork failures. Nontechnical skills such as communication, cooperation, and coordination are critical components of teamwork, but limited interpersonal skills can underlie patients' sudden movements and adverse events [22], [23]. These sudden movements are typically challenging to predict and react accordingly. In manual surgery, surgeons rest their hands directly on the patient's head, naturally establishing a connection between their hands and the head. This practice enables them to compensate for any undesired movement from any source. This immediate error detection and compensation help prevent complications during surgery. On the other hand, in robotic surgery, there is no direct hand-forehead coupling. Regardless of the source, any patient motion and head shift can lead to an error. These robotic systems rarely account for the effects of patient motion. Therefore, all clinically deployed robotic systems for vitreoretinal surgery must address patient motion independently, regardless of source. Motion analysis stands as a cornerstone in modern engineering and surgical fields [24], offering invaluable insights into the behavior of mechanical systems and their impact on performance. Its importance is magnified when applied to delicate and high-precision contexts, such as robotic systems used in vitreoretinal surgery. In these surgical procedures, where precision and accuracy are paramount, understanding and mitigating vibrations at the robotic system's end-effector is critical to achieving successful outcomes and safeguarding patient well-being.

In the proposed project, four IMUs are strategically placed in a grid layout on the environmental or the object of interest, as shown in Fig. 1. This grid layout ensures that motion and vibration data can be captured simultaneously from various points on the object. The spacing and distribution of sensors in the grid layout are crucial to accurately capture the full range of movement. This arrangement aims to optimize data collection and coverage and ensure the sensors effectively capture relevant motion information from their monitoring environment. The grid design, illustrated in Fig. 1, helps us collect all motion on two vital robot-instrument nodes (**node0**) and Patient Head node (**node1**), and the motion from other areas which can affect these two nodes during the surgery. All the data collected by the sensors in the grid is then fused and processed. Combining the data from all the sensors, the system can comprehensively represent the patient's and robot's motion, including large movements and subtle vibrations. At the same time, in a parallel branch with a Recurrent Neural Network, any coming motion at the robot's final axis (node0) caused by motions at other nodes is predicted.

II. Related Work

To date, only a few published works share the idea of intraoperatively analyzing and compensating undesired motions. Most of the studies that have been done involve a completely stationary eye or an eye with a simple rotation. Incorporating these sudden motions into other developmental tasks adds more complexity to all experiments. Furthermore, generating actual mechanical motion poses a significant challenge.

One mitigation solution is enabling passive approaches to minimize sudden patient head motion at a final contact point. One approach is limiting the patient's head by introducing a headrest mechanism to decrease the head motion to below 9 mm [25]. One step further is to mitigate the head motion by enabling the semirigid connection between the robot and patient head [12], [26]. Edwards et al. [27] proposed another passive approach to bypass the head motion by attaching an adopter to the standard valved trocar in the sclera. These methods can reduce head motion; however, their benefits in delicate vitreoretinal surgeries still need to be quantified. On the other hand, mounting the robot on the head is challenging and requires sensitive dealing with the patient's skull. Closed-loop compensation solutions offer active detection

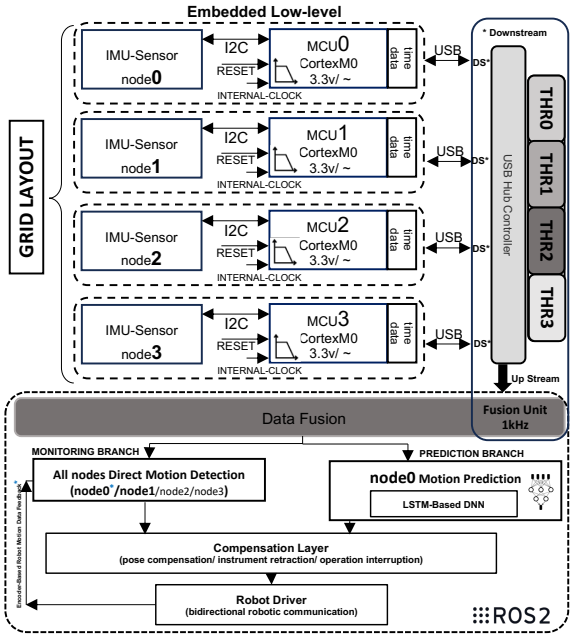

Fig. 2. An overall architecture of the system.

and appropriate reaction. Active compensation can involve sensing the force between the surgical instrument and the eye [28]–[30]. Force sensors are commonly used for sensitive measurement of intraoperative extrusion to detect hazardous interactions during tool-tissue interaction. However, combining force feedback with kinematic optimization remains a challenging task. Furthermore, incorporating force sensors into surgical instruments introduces additional complexities, such as the need for certification and compliance with clinical requirements. Utilizing visual-servoing and image-based approaches [31] is another sudden motion compensation method. The bottleneck of these approaches for fast and accurate motion detection requires high-frame-rate image extraction, expensive computations, and complex calibrations.

Another active compensation idea is utilizing an interactive headrest to move the head concerning any undesired motion. Natalius et al. [27] designed a parallel robotic system to act as a headrest that ultimately counteracts patient motion. This proposed design has the potential to simulate patient motion, but its responsiveness has not been thoroughly investigated.

Most robotic systems used in micro-surgery applications, including robotic vitreoretinal procedures, are characterized by rigid structural configurations. Consequently, in the scope of this research, we define motion as alterations in linear acceleration and angular velocities. To achieve a comprehensive understanding of six-dimensional (6D) environmental motion at a high frequency, we employ a network of Internal Measurement Units (IMUs). The grid layout is instrumental in gathering motion data from multiple points, which can influence the motion of two critical nodes, Node0 and node1, during the surgical procedure. As illustrated in Fig. 2, within the embedded low-level section, data packets containing motion details and their respective timestamps are transmitted via distinct threads (THR0-3). Once all the data from various nodes is combined into a motion data array, the system initiates two parallel branches. In the first branch, all motions of each node are closely monitored in real time. The second branch takes a more proactive approach. It uses a deep neural network to predict motion based on real-time data from all nodes. This prediction helps to anticipate any upcoming motion or vibrations at node0, which actions in other places can cause. We specifically focus on predicting motion at node0, while we assume it is an objective measure and originates from motions elsewhere. In the subsequent stage of the method, the outputs of these two branches are channeled into the compensation layer. Here, the robot's reaction is adjusted, which may involve actions like the robot's position compensation, instrument retraction, or even halting the robot's operation. For example, if the identified motion surpasses a pre-established threshold, a signal is transferred to the robot to perform needle retraction.

III. Method

A. 6D Motion Analysis

6D motion is calculated by utilizing a triaxial accelerometer that measures linear acceleration along three axes, while a triaxial gyroscope measures angular velocity. (Fig. 3-c). In this definition, by calculating a reference point, all changes in linear acceleration and angular velocity are analyzed. In order to remove all offsets and calculate the reference point, for all 6-axes, many measurements (k) are done, and an average of these data points is considered as a reference value (ref_v) when the system is stationary. In the Eq. 1, v is representative of all 6D ($acc_x, acc_y, acc_z, gyr_{\theta x}, gyr_{\theta y}, gyr_{\theta z}$) data respectively.

$$ref_v = \frac{\sum_{j=1}^{k} v\,(t_j)}{k} \Rightarrow \Delta v_t = v_t - ref_v \tag{1}$$

After calculating all changes in acceleration in ($\frac{mm}{s^2}$) and angular velocity in ($\frac{deg}{s}$), a motion vector (represents as $\vec{v}$) is defined to represent the acceleration ($\vec{ac}_{lin}$) and velocity ($\vec{ve}_{ang}$) for each node. These vectors for each node are calculated using Eq. 2 separately, where $\|\Delta v_t\|$ is the magnitude of the vector, and direction angles are named α(x-axis), β(y-axis) and γ(z-axis).

$$\|\Delta v_t\| = \sqrt{(\Delta vx_t^2) + (\Delta vy_t^2) + (\Delta vz_t^2)} \quad \alpha{=}\cos^{-1}\left(\tfrac{\Delta vx_t}{\|\Delta v_t\|}\right), \beta{=}\cos^{-1}\left(\tfrac{\Delta vy_t}{\|\Delta v_t\|}\right), \gamma{=}\cos^{-1}\left(\tfrac{\Delta vz_t}{\|\Delta v_t\|}\right) \tag{2}$$

B. Motion Calculation

The variation in position (ΔP_{lin}) along each axis over a defined time (t) by considering linear acceleration (Δa_{lin}) is computed by Eq. 3, assuming an initial velocity of zero.

$$\Delta P_{lin} = \frac{1}{2}\Delta a_{Lin} \times t^2 \tag{3}$$

Similarly, the total difference in rotational and then positional movement using angular velocity (Δv_{ang}) is calculated by Eq.4. An angular difference Δ_θ is converted to positional displacement along a circular path with the radius of R.

$$\Delta_\theta = \frac{\pi}{180}\Delta v_{ang} \times t \Rightarrow \Delta P_{ang} = \Delta_\theta \times R \tag{4}$$

C. Network Architecture

An LSTM-based (Long Short-Term Memory) neural network [32] is employed for motion prediction. LSTM belongs to the recurrent neural networks (RNNs) category and can capture long-term dependencies within sequential data (Fig. 4). LSTM networks possess a distinct architecture featuring a cell and three gates: **input**, **output**, and **forget**. The cell retains information across time steps, while the gates govern the amount of information to retain, discard, or output from the cell. To train this network, we curated a tailored dataset encompassing 6D vibration data from all nodes operating within an environment characterized by random vibrations. This dataset comprises a training set comprising 100,000 instances of motion data from all nodes and a validation set containing 10,000 motion data samples.

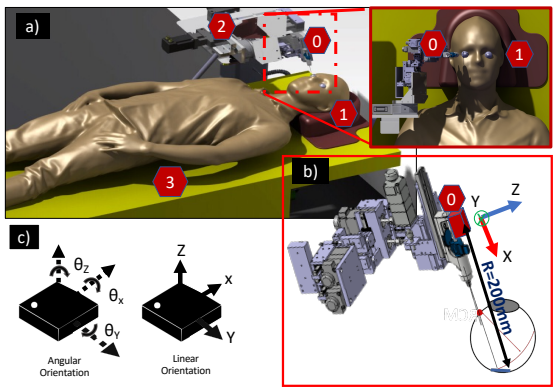

Fig. 3. (a) Shows an overview of the sensors' placement in the grid layout. (b) Exhibits the sensor placement on node0 (the robot's final axis), and (c) presents the calculation of linear acceleration and angular velocity extracted by the IMU sensor.

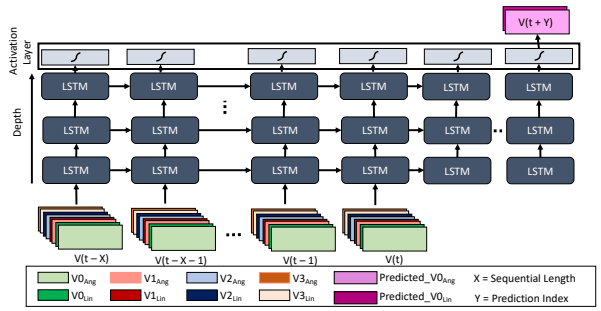

Fig. 4. The stacked LSTM sequence-to-sequence architecture predicts 6D motion at node0 at $t+Y$ as a result of 6D motion data at all nodes between $t-X$ to t; Detailed description of the notations in Sec. III-C.

D. Pearson Correlation

The Pearson correlation coefficient, or Pearson's measures the linear correlation between variable pairs [33]. This measure is commonly used to explore relationships between two time-series data. Given a set of paired samples, D_1, $D_2 \subseteq \mathbb{R}^N$, the Pearson correlation coefficient is defined as,

$$r = \frac{cov(D_1, D_2)}{\sqrt{var(D_1)var(_D2)}} \tag{5}$$

wherein $var(\cdot)$ and $cov(\cdot)$ denote sample variance and covariance of the respective random samples. With a range of $(-1, 1)$, Pearson correlation indicates correlation $+1$, anti-correlation -1, or the absence of correlation 0. It is easy to interpret, quantifying the strength and direction of the relationship between the actual and predicted data. However, caution is needed when the relationship is nonlinear or when outliers are present, as they can significantly affect the correlation coefficient.

E. Mean Absolute Percentage Error (MAPE)

MAPE is a commonly used metric for analyzing the accuracy of forecasts or predictions in time-series data [34]. It quantifies the percentage difference between the predicted and actual values, measuring how well a model or forecasting method performs. It usually expresses the accuracy as a ratio.

IV. Materials

For our experiments, we used a setup consisting of *5DOF robot* proposed by Nasseri et al. [12], a *Head rest module*, and four *MPU6050 sensors* to calculate 6D motions and vibrations (Fig. 1). Both robot and sensors grid are connected to a workstation with a USB interface and communicate with ROS2[1] [35] as illustrated in Fig. 2.

V. Experiments and Results

A. 6D Motion Data Readout

The embedded low-level unit, illustrated in Fig. 2, is responsible for managing hardware and essential functions, which are critical for the system's operation, such as initiating the sensor and micro-controller unit (MCU), configuring UART/USB communication, carrying out calibration, and conducting low-level data retrieval from each sensor via the I2C protocol. In the first step, we set the dynamic range of all sensors in a full-scale range of $\pm 19600 mm/s2$, $\pm 250 deg/s$ in linear acceleration and angular velocity, respectively. With these parameters, we limited our detection range to the mentioned values and, as a result, achieved the highest sensitivity of $1.67 mm/s$ and $0.00769 deg/s$ in each sensor by processing 16-bit data for each axis. Additionally, we implemented Digital Low Pass Filters (DLPF) with a cut-off frequency set at 260 *Hz* for acceleration data and 265 *Hz* for velocity data. This configuration effectively appointed our sample rate at 1 *kHz* for each sensor. It is worth mentioning that this range of motion detection in delicate robot-assisted surgeries, such as vitreoretinal surgery with a desired low motion and high sensitivity, is entirely acceptable. As elaborated in Sec. III-A, it is imperative to calibrate all sensors in order to eliminate any offsets and determine reference values for all six axes. This calibration procedure initiates immediately after initializing the sensors and takes 30 seconds, involving 2000 data retrievals. Following data retrieval from each node, the data is encapsulated in an array format, including linear accelerations and angular velocities, complete with a unique header and tail for each sensor, before being transmitted. This method is implemented on the Ubuntu Linux distribution as the operating system, and the next step is analyzing the USB communication Network. Therefore, we investigated the data packets from USB Hub to the Linux kernel using the WireShark tool [36]. This experiment helps us to analyze that the data packets stream is transmitting correctly between the upstream side till the Linux Kernel at the desired frequency and lowest lost packets. During this time frame, we monitored that the data transmission frequency remained consistent across two data ports, and there were no instances of lost data packets.

B. Real-time Data Analyzing

After receiving each packet from all sensors, we start fusing them through different threads using ROS 2. In this step, we must ensure the fused motion data is completely synced and real-time. Since the node0 IMU is physically attached to the robot's Z-axis (final Axis, shown in Fig. 1, and Fig. 3), we leverage employing the highly precise encoder (with an accuracy within $0.1 \mu m$) assembled on each robot's actuator as ground truth. Therefore, the robot's movement is expected to create motion simultaneously at the part of the fused data correlated with node0. In order to complete this experiment, we designed a rectangular trajectory experiment. In this experiment, the robot was moved translationally within a rectangular trajectory. It initiated its motion from a predefined starting point, with the highest velocity of 1 mm/s along two orthogonal axes, namely the X and Y axes. This experiment comprised four cycles. Within each cycle, the robot is stopped for 2000 ms, then the robot is directed to run translational movements for 500 ms. After this active movement phase, a command was given to halt the robot's motion for 2500 ms, thus introducing a controlled pause,

[1]https://github.com/ros2

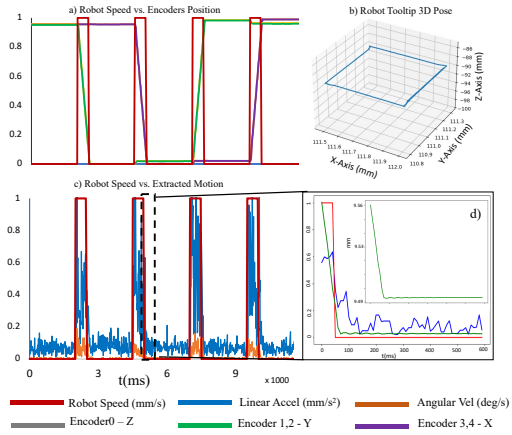

Fig. 5. Analysis of the real-time readout by comparing the encoder data and the motion information segment in the fused data in the rectangular trajectories experiment. (a) a comparing plot of binary scaled values of the robot's encoder to the robot's speed. (b) the 3D view of the calculated robot's end-effector (tooltip) by employing forward kinematic [37], (c) the robot's speed vs. motion profile of the node0, and (d) anticipates the zoomed-in view of the stop command in the second cycle.

before initiating the subsequent cycle.

We analyzed the encoder data stop/start command and received motion data in both experimental scenarios. The results show precise synchronization between the robot's movements and the motion data captured by the sensors, and the robot's stop mode (mechanically fixing all joints) eliminates all extracted motion in node0. Given that the communication rate for robot commands is set at 100 *Hz*, which is ten times lower than the rate of motion extraction, our experimental findings indicate that data latency is almost neglectable, as illustrated in Fig. 5, which shows that the latency of our method is less than 10 ms.

C. Tooltip Motion Estimation Analysis

Calculating the positional motion of the tooltip, denoted as Δp_{tip}, is closely linked to the motion pattern of node0. This relationship arises from the rigid nature of the instrument and the minimal distance (R) between the final axis of the robot (node0) and the tooltip. Given that instruments used in micro-surgical procedures like vitreoretinal surgery typically have tiny dimensions on the sub-millimeter scale, we can safely disregard the impact of node0 angular motion in the X-Axis (as illustrated in Fig. 3-a). Furthermore, we have assumed that the trocar's damping factor (α) is approximately 0. Consequently, the calculation of the tooltip's position based on the linear and angular motion profile of node0 is determined by Eq. 6, where $\Delta P0_{lin}$ and $\Delta P0_{Ang}$ are calculated by Eq. 3 and Eq. 4 respectively, and R is 200 mm (See Fig. 3).

$$\Delta_{Ptooltip} = (1-\alpha)\Delta P0_{lin} + \Delta P0_{Ang}|_{(\Delta Gyr_x=0)} \quad (6)$$

To obtain high-frequency motion data from the tooltip, we attached a small and lightweight IMU sensor to the tooltip, as displayed in Fig. 6. Given that the sensor weighs only 1.8 grams and is pre-calibrated with 2000 data points before sampling, the effects of counterweight and wiring were negligible. During this experiment, we collected motion data, including 1,900 data points, each sampled at a rate of 100 *Hz* and generated with random motion patterns, and subsequently calculated the tooltip's motion using Eq. 6. We then compared these calculated results with the data recorded by the attached sensor at the tooltip. Furthermore, We have calculated the MAPE index to evaluate the point-to-point error percentage. The resulting MAPE value is 13%, which can be considered an acceptable range given the underlying assumptions and small range of motions.

D. Motion Prediction

The transmission of motion from one location to another via mechanical wave propagation is influenced by various physical factors, including distance, material properties, and the configuration of the robot's structure. Consequently, for motion prediction by using a neural network, discovering the optimized setup-based parameters, such as X and Y, which are representative of the length of input data and time index of upcoming motion, as described in Sec. III-C, is a critical step, to train the network with the highest efficiency and lowest inference time.

1) Optimized Parameter Analysis: The network was trained using various X and Y values to identify these optimal parameters and evaluate the influence of input array length (X) and prediction index (Y). The experimentation involved a range of values for X and Y, spanning from 100 to 450 data points in increments of 50 for X and from 10 to 90 data points with 5-unit increments for Y for a total of 133 networks. Subsequently, the performance of all trained networks was assessed using an unseen dataset comprising 80,000 data points, randomly generated from diverse sources. Thereafter, we gathered all outcomes and conducted a comparative analysis by node0 at $t + Y$ (as ground truth). The comparison involved evaluating the Mean Absolute Percentage Error (MAPE), Pearson correlation metrics, and inference time indices. The inference time for all trained networks, when applied to each fused motion data

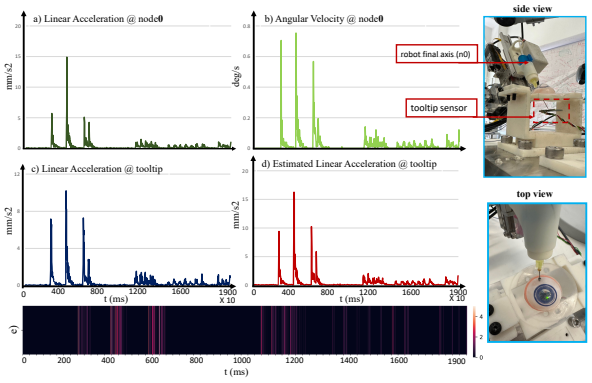

Fig. 6. Experiments on 1900 different vibrations at node0 (a,b), comparing the actual experienced motion (c) and estimated vibration using Eq. 6(d). On the right, it shows how the sensor is assembled at the tooltip. (e) shows the point-to-point acceleration difference heat map between estimation and sensor data.

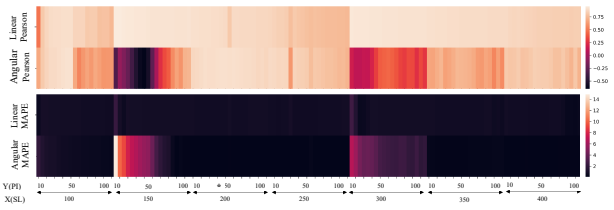

Fig. 7. The MAPE and Pearson correlation index for all trained DNNs with different trained X, Y values.

array ($[t - X : t]$), remains consistently within the range of 1.33 to 4.5 milliseconds. Upon a thorough comparison of all the outcomes, as illustrated in Fig. 7, we selected 200 as the value for parameter X and 40 for parameter Y. This selection provided a 40 milliseconds forecast of future motion using data from the preceding 200 milliseconds. The analysis results show a MAPE of 2 and a Pearson correlation coefficient of 0.98.

2) Training: The models are trained with X, Y as sequential length and prediction index (X, Y in Sec. III-C) and hidden size equal to 64 to optimize the L1 loss as a similarity measure, with L2 loss yielding similar results in our experiments. We use the Adam optimizer [38] with an initial learning rate of 1×10^{-6} and 256 samples per batch. An adaptive learning rate scheduler reduces the learning rate by a factor of 0.1, and the network is trained for 500 epochs.

3) Dependency on each Node: In this experimental investigation, we analyzed the influence of individual nodes on the accuracy of predictions. As previously elaborated in Sec. V-D.1, we configured the prediction index to be 50. It is worth remembering that the network's response varies depending on the source of vibration. Following a thorough examination

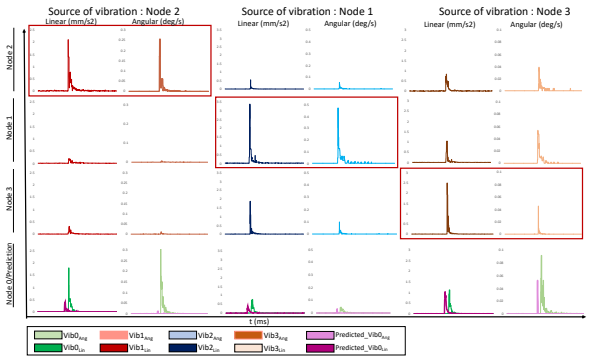

Fig. 8. Presents how sensitive the network prediction is to motion coming from different nodes.

of the network's prediction outcomes in the result of the unseen data, which is presented in Fig. 8, it becomes noticeable that the prediction network shows limited capability in accurately forecasting motion originating from node2 (Robot's Frame, Fig. 8-a), in contrast of higher sensitivity indication to motion sourced from other nodes (node1 and node3, Fig. 8-b,c). This observation reflects the network's efficiency, which depends on the grid's physical configuration. It derives from the relative distances between node0 (the primary node) and node2 (the robot's frame), compared to the distances between two other nodes and node0. In this context, the proximity of node2 to node0 is notably closer than the distances separating node0 from node1 and node3. This distance difference is crucial in shaping the network's ability to accurately predict motions from different sources. Given the constraints related to speed and response latency within the micro-surgical robotic platform, obtaining motion predictions slightly in advance, even by just a few milliseconds, at critical joints can hold significant value. Nevertheless, this approach tends to be less dependable when it comes to analyzing motion originating from close distances within such a rigid structural setup. To address these challenges effectively, the second branch dedicated in Fig. 2 can be a potential solution that involves acquiring real-time motion data for nearby nodes.

4) Inference Rate: With inference on an NVIDIA GeForce RTX A5000, we measured an average inference time of 0.002 ± 0.0008 seconds for each point motion prediction at **node0** (Fig. 2).

VI. Discussion and Future Work

The present work characterized passive motion and vibration as undesired alterations in linear and angular acceleration and velocity within rigid mechanical structures focusing on micro-surgical robotic platforms. It allows to estimation of undesired motions of the system and concentrates on the controlled and precise movements affecting the stability and accuracy of these mechanical systems. By concentrating on rigid structures, we intentionally exclude the consideration of non-rigid objects like fluids, gases, or deformable solids. These materials exhibit motion in various forms, driven by factors like pressure, density, or shape changes. Examples include phenomena like sound waves, shock waves, or elastic waves. These waves propagate through a medium featuring variable frequencies and amplitudes. The rationale lies in the specific focus of the study using a micro-surgical robotic platform. In this context, understanding and mitigating motion within rigid components is crucial. By narrowing the scope to rigid structures, we can provide more effective solutions for the challenges encountered in this domain without the complexities introduced by non-rigid motions. This focused approach allows the delivery of robust and actionable understandings for enhancing the performance and reliability of micro-surgical robotic systems. Within the community, another crucial area of concern is motion requirements to design the compensation layer and the decision-making process. Once we have accurately calculated the motion within the final node, it becomes evident that establishing standardized thresholds and considering surgical phase dynamics are two pivotal factors demanding our collective attention in future research.

VII. Conclusion

This paper introduces an advanced motion and vibration analysis network for real-time monitoring in all regions that could affect the defined node's motion. The network utilized in this system operates at a high frequency, ensuring the delivery of accurate and timely data.

REFERENCES

[1] S. Dehghani, M. Sommersperger, P. Zhang, A. Martin-Gomez, B. Busam, P. Gehlbach, N. Navab, M. A. Nasseri, and I. Iordachita, "Robotic navigation autonomy for subretinal injection via intelligent real-time virtual ioct volume slicing," *arXiv preprint arXiv:2301.07204*, 2023.

[2] Y. Zhao, A.-M. Jablonka, N. A. Maierhofer, H. Roodaki, A. Eslami, M. Maier, M. A. Nasseri, and D. Zapp, "Comparison of robot-assisted and manual cannula insertion in simulated big-bubble deep anterior lamellar keratoplasty," *Micromachines*, vol. 14, no. 6, p. 1261, 2023.

[3] J. W. Kim, P. Zhang, P. Gehlbach, I. Iordachita, and M. Kobilarov, "Micromanipulation in surgery: Autonomous needle insertion inside the eye for targeted drug delivery," *arXiv preprint arXiv:2306.17421*, 2023.

[4] ——, "Deep learning guided autonomous surgery: Guiding small needles into sub-millimeter scale blood vessels," *arXiv preprint arXiv:2306.10133*, 2023.

[5] A. Molaei, E. Abedloo, M. D. de Smet, S. Safi, M. Khorshidifar, H. Ahmadieh, M. A. Khosravi, and N. Daftarian, "Toward the art of robotic-assisted vitreoretinal surgery," *Journal of ophthalmic & vision research*, vol. 12, no. 2, p. 212, 2017.

[6] A. Alikhani, S. Oßner, S. Dehghani, B. Busam, S. Inagaki, M. Maier, N. Navab, and M. A. Nasseri, "Rcit: A robust catadioptric-based instrument 3d tracking method for microsurgical instruments in a single-camera system."

[7] N. A. Maierhofer, A.-M. Jablonka, H. Roodaki, M. A. Nasseri, A. Eslami, J. Klaas, C. P. Lohmann, M. Maier, and D. Zapp, "ioct-guided simulated subretinal injections: a comparison between manual and robot-assisted techniques in an ex-vivo porcine model," *Journal of Robotic Surgery*, pp. 1–8, 2023.

[8] M. N. Menke, S. Dabov, P. Knecht, and V. Sturm, "Reproducibility of retinal thickness measurements in healthy subjects using spectralis optical coherence tomography," *American journal of ophthalmology*, vol. 147, no. 3, pp. 467–472, 2009.

[9] C. Creveling, Y. Alsanea, and B. Coats, "Correlation of collagen fibril properties and inner limiting membrane thickness with vitreoretinal adhesion in human eyes," *Experimental Eye Research*, vol. 223, p. 109189, 2022.

[10] T. Sakai, K. Harada, S. Tanaka, T. Ueta, Y. Noda, N. Sugita, and M. Mitsuishi, "Design and development of miniature parallel robot for eye surgery," in *2014 36th Annual International Conference of the IEEE Engineering in Medicine and Biology Society*. IEEE, 2014, pp. 371–374.

[11] A. Gijbels, K. Willekens, L. Esteveny, P. Stalmans, D. Reynaerts, and E. B. Vander Poorten, "Towards a clinically applicable robotic assistance system for retinal vein cannulation," in *2016 6th IEEE International Conference on Biomedical Robotics and Biomechatronics (BioRob)*. IEEE, 2016, pp. 284–291.

[12] M. A. Nasseri, M. Eder, S. Nair, E. C. Dean, M. Maier, D. Zapp, C. P. Lohmann, and A. Knoll, "The introduction of a new robot for assistance in ophthalmic surgery," in *Eng. Med. Biol. Soc. (EMBC), 2013 35th Annu. Int. Conf. IEEE*. IEEE, 2013, pp. 5682–5685.

[13] A. Gijbels, N. Wouters, P. Stalmans, H. Van Brussel, D. Reynaerts, and E. Vander Poorten, "Design and realisation of a novel robotic manipulator for retinal surgery," in *2013 IEEE/RSJ International Conference on Intelligent Robots and Systems*. IEEE, 2013, pp. 3598–3603.

[14] E. Vander Poorten, C. N. Riviere, J. J. Abbott, C. Bergeles, M. A. Nasseri, J. U. Kang, R. Sznitman, K. Faridpooya, and I. Iordachita, "Robotic retinal surgery," in *Handbook of robotic and image-guided surgery*. Elsevier, 2020, pp. 627–672.

[15] C. Bergeles, M. Sugathapala, and G.-Z. Yang, "Retinal surgery with flexible robots: Biomechanical advantages," in *2018 International Symposium on Medical Robotics (ISMR)*, 2018, pp. 1–6.

[16] H. Meenink, G. Naus, M. J. Beelen, M. Steinbuch, P. Rosielle, and M. D. de Smet, "Ex-vivo experiments with a microrobotic surgical system for vitreo-retinal surgery," in *conference; Annual meeting: Association for Research in Vision and Ophthalmology; 2012-05-05; 2012-05-11*, 2012.

[17] Y. Koyama, M. M. Marinho, and K. Harada, "Vitreoretinal surgical robotic system with autonomous orbital manipulation using vector-field inequalities," in *2023 IEEE International Conference on Robotics and Automation (ICRA)*, 2023, pp. 4654–4660.

[18] J. Salmon, B. Mets, M. James, and A. Murray, "Intravenous sedation for ocular surgery under local anaesthesia." *British journal of ophthalmology*, vol. 76, no. 10, pp. 598–601, 1992.

[19] K. Brogan, B. Dawar, D. Lockington, and K. Ramaesh, "Intraoperative head drift and eye movement: two under addressed challenges during cataract surgery," *Eye*, vol. 32, no. 6, pp. 1111–1116, 2018.

[20] C. A. Mccannel, E. J. Olson, M. J. Donaldson, S. J. Bakri, J. S. Pulido, and M. Donna, "Snoring is associated with unexpected patient head movement during monitored anesthesia care vitreoretinal surgery," *Retina*, vol. 32, no. 7, pp. 1324–1327, 2012.

[21] J. A. Wahr, R. L. Prager, J. Abernathy Iii, E. A. Martinez, E. Salas, P. C. Seifert, R. C. Groom, B. D. Spiess, B. E. Searles, T. M. Sundt III *et al.*, "Patient safety in the cardiac operating room: human factors and teamwork: a scientific statement from the american heart association," *Circulation*, vol. 128, no. 10, pp. 1139–1169, 2013.

[22] K. Mazzocco, D. B. Petitti, K. T. Fong, D. Bonacum, J. Brookey, S. Graham, R. E. Lasky, J. B. Sexton, and E. J. Thomas, "Surgical team behaviors and patient outcomes," *The American Journal of Surgery*, vol. 197, no. 5, pp. 678–685, 2009.

[23] D. Shouhed, B. Gewertz, D. Wiegmann, and K. Catchpole, "Integrating human factors research and surgery: a review," *Archives of Surgery*, vol. 147, no. 12, pp. 1141–1146, 2012.

[24] G. Forestier, F. Petitjean, P. Senin, F. Despinoy, A. Huaulmé, H. I. Fawaz, J. Weber, L. Idoumghar, P.-A. Muller, and P. Jannin, "Surgical motion analysis using discriminative interpretable patterns," *Artificial intelligence in medicine*, vol. 91, pp. 3–11, 2018.

[25] K. Huang, M. Zhou, C. Lajblich, C. P. Lohmann, A. Knoll, Y. Ling, H. Lin, and M. A. Nasseri, "A flexible head fixation for ophthalmic microsurgery," in *2017 Chinese Automation Congress (CAC)*. IEEE, 2017, pp. 6707–6710.

[26] M. A. Nasseri, M. Maier, and C. P. Lohmann, "A targeted drug delivery platform for assisting retinal surgeons for treating age-related macular degeneration (amd)," in *2017 39th annual international conference of the IEEE Engineering in Medicine and Biology Society (EMBC)*. IEEE, 2017, pp. 4333–4338.

[27] T. Edwards, K. Xue, H. Meenink, M. Beelen, G. Naus, M. Simunovic, M. Latasiewicz, A. Farmery, M. De Smet, and R. MacLaren, "First-in-human study of the safety and viability of intraocular robotic surgery," *Nature biomedical engineering*, vol. 2, no. 9, pp. 649–656, 2018.

[28] A. Ebrahimi, M. G. Urias, N. Patel, R. H. Taylor, P. Gehlbach, and I. Iordachita, "Adaptive control improves sclera force safety in robot-assisted eye surgery: A clinical study," *IEEE Transactions on Biomedical Engineering*, vol. 68, no. 11, pp. 3356–3365, 2021.

[29] X. He, J. Handa, P. Gehlbach, R. Taylor, and I. Iordachita, "A sub-millimetric 3-dof force sensing instrument with integrated fiber bragg grating for retinal microsurgery," *IEEE Transactions on Biomedical Engineering*, vol. 61, no. 2, pp. 522–534, 2013.

[30] C. Gruijthuijsen, L. Dong, G. Morel, and E. V. Poorten, "Leveraging the fulcrum point in robotic minimally invasive surgery," *IEEE Robotics and Automation Letters*, vol. 3, no. 3, pp. 2071–2078, 2018.

[31] B. C. Becker, R. A. MacLachlan, L. A. Lobes, G. D. Hager, and C. N. Riviere, "Vision-based control of a handheld surgical micromanipulator with virtual fixtures," *IEEE Transactions on Robotics*, vol. 29, no. 3, pp. 674–683, 2013.

[32] S. Hochreiter and J. Schmidhuber, "Long short-term memory," *Neural computation*, vol. 9, no. 8, pp. 1735–1780, 1997.

[33] I. Cohen, Y. Huang, J. Chen, J. Benesty, J. Benesty, J. Chen, Y. Huang, and I. Cohen, "Pearson correlation coefficient," *Noise reduction in speech processing*, pp. 1–4, 2009.

[34] A. De Myttenaere, B. Golden, B. Le Grand, and F. Rossi, "Mean absolute percentage error for regression models," *Neurocomputing*, vol. 192, pp. 38–48, 2016.

[35] S. Macenski, T. Foote, B. Gerkey, C. Lalancette, and W. Woodall, "Robot operating system 2: Design, architecture, and uses in the wild," *Science Robotics*, vol. 7, no. 66, p. eabm6074, 2022.

[36] C. Sanders, *Practical packet analysis: Using Wireshark to solve real-world network problems*. No Starch Press, 2017.

[37] M. W. Spong, S. Hutchinson, M. Vidyasagar *et al.*, *Robot modeling and control*. Wiley New York, 2006, vol. 3.

[38] D. P. Kingma and J. Ba, "Adam: A method for stochastic optimization," *arXiv preprint arXiv:1412.6980*, 2014.